PROCEEDINGS, 50th Workshop on Geothermal Reservoir Engineering
Stanford University, Stanford, California, February 10-12, 2025
SGP-TR-229

Characterizing In-Situ Stresses at Utah FORGE Using a Multi-Component Approach Combining Laboratory Experiments, Field Measurements, Physics-Based Modeling, and Machine Learning Methods

Guanyi Lu[1], Ayyaz Mustafa[1], Andrew P. Bunger[1,2]

1 Department of Civil and Environmental Engineering, University of Pittsburgh, Pittsburgh, PA, USA

2 Department of Chemical and Petroleum Engineering, University of Pittsburgh, Pittsburgh, PA, USA

gul51@pitt.edu, aym40@pitt.edu, bunger@pitt.edu

Keywords: In-Situ Stress Estimation, Enhanced Geothermal Systems, Utah FORGE, Velocity-to-Stress Correlation, Stress-Induced Wave Speed Anisotropy, Core-Based Laboratory Experiments, Field Measurements, Physics-Based Modeling, Machine Learning

ABSTRACT

This study presents a novel multi-component approach that combines core-based laboratory triaxial ultrasonic velocity (TUV) experiments, field measurements, machine learning (ML) models, and physics-based finite element simulations to characterize in-situ principal stresses near a geothermal well. Laboratory TUV experiments were conducted on core samples from well 16A(78)-32 at Utah FORGE under true-triaxial stress conditions to establish velocity-to-stress relationships. These relationships were then used to develop ML models that predict near-field stresses based on sonic logging data. While the ML predictions successfully estimate the three principal stresses, near-wellbore stress concentrations and thermo-poro-elastic disturbances induced by drilling and pre-cooling significantly influence the results. To address this, we coupled the ML derived stresses with a physics-based thermo-poro-mechanical finite element model to translate near-field stresses into far-field stresses. Simulations account for realistic pre-cooling and warmup scenarios, material properties, and boundary conditions to quantify stress evolution near geothermal wells. Results demonstrate the critical impact of thermal effect on stress distributions, with notable stress variations observed near the borehole that diminish radially. Moreover, thermo-poro-mechanical effect amplifies the difference between the two horizontal principal stresses in the near-field. Therefore, the undisturbed far-field stresses are generally more isotropic than near-field predictions. The integration of laboratory and field measurements, ML predictions, and physics-based modeling provides a robust framework for accurately characterizing far-field stresses in geothermal reservoirs. The findings have significant implications for the development and optimization of enhanced geothermal systems and other subsurface energy applications.

1. INTRODUCTION

Estimating in-situ stress in subsurface rock formations is critical for various energy and geotechnical applications, including hydraulic fracturing, wellbore stability, and geothermal energy exploitation (Zang and Stephansson, 2009). Traditional field-based stress measurement techniques, such as injection tests and thermo-poro-mechanical models, face significant limitations. These methods are often costly, time-intensive, and provide stress data only at discrete depths rather than continuous profiles. Moreover, indirect methods for determining maximum horizontal stress rely on constitutive assumptions with certain restrictions. These challenges are further exacerbated in geothermal reservoirs. In-situ stress testing is particularly difficult to perform and interpret in enhanced geothermal systems (EGS) because of the extreme temperatures that complicate measurements and require specialized and expensive equipment. This necessitates the use of specialized equipment and/or pre-cooling of a wellbore, both of which can increase operating costs and, in the case of pre-cooling, cause a thermal stress disturbance that complicates data interpretation (Lu et al., 2024a).

To overcome these limitations, there is a growing need for reliable, cost-effective stress characterization methods that can provide continuous profiles along the entire depth of a wellbore. Recent advancements in artificial intelligence (AI) and machine learning (ML) offer promising alternatives. By integrating ML technologies, Mustafa et al. (2024) utilized a data-driven approach to predict subsurface features and stresses based on logging data. The predicative ML model, trained by laboratory triaxial ultrasonic velocity (TUV) data (Bunger et al., 2024), effectively captured the constitutive relationship between the slowness of three ultrasonic waves - compressional (P-)wave and fast and slow shear (S-)waves - and the applied principal stresses in rock samples. The optimized models were then applied to field sonic log data to predict the three principal stresses sequentially. Complementing this data-driven approach, a physics-based finite element model was constructed in Abaqus to simulate the stress field near an EGS well (Lu et al., 2024b). This model accounts for critical thermo-poro-mechanical effects associated with thermal and pore pressure diffusion during operations like drilling and borehole pre-cooling circulations. Notably, the results highlight significant thermal stress alterations caused by extensive pre-cooling operations.

In this study, we present a novel multi-component approach that integrates all the above-mentioned methods (i.e., core-based laboratory TUV testing, field measurements, ML techniques, and physics-based modeling) for characterizing the magnitude of in-situ stresses near a geothermal well. Central to our methodology is the so-called velocity-to-stress correlation in rocks (Sinha and Kostek, 1996; Prioul et al., 2004). Both field evidence and lab measurements indicate the presence of stress-induced wave speed anisotropy in FORGE rocks (Bunger et al., 2024). The differences in the in-situ principal stresses would lead to varying wave velocities depending on the wave type, propagation direction, and polarity relative to the principal stress orientations. The core-based laboratory TUV testing builds on this

understanding by leveraging rocks' stress dependence of wave velocities to generate a robust dataset for developing optimized ML models. Unlike prior studies constrained by specific constitutive laws, the large amount of testing data ensures the development of reliable ML models to determine the velocity-to-stress correlation given the wave speeds in certain rock types using well log data. Physics-based modeling further extends the near-field stress predictions to far-field while incorporating thermo-poro-elastic stress disturbances. Using this integrated approach, we characterize the stress distribution at well 16A(78)-32 of Utah FORGE EGS project, providing a comprehensive framework for in-situ stress estimation in complex geothermal reservoirs.

2. METHODOLOGY

The methodology is divided into three main steps: (1) conducting core-based TUV experiments, (2) developing and applying velocity-to-stress ML models to estimate near-field principal stresses, and (3) utilizing physics-based finite element model to characterize far-field stresses under significant thermo-poro-mechanical effects. The overall workflow is summarized in Figure 1.

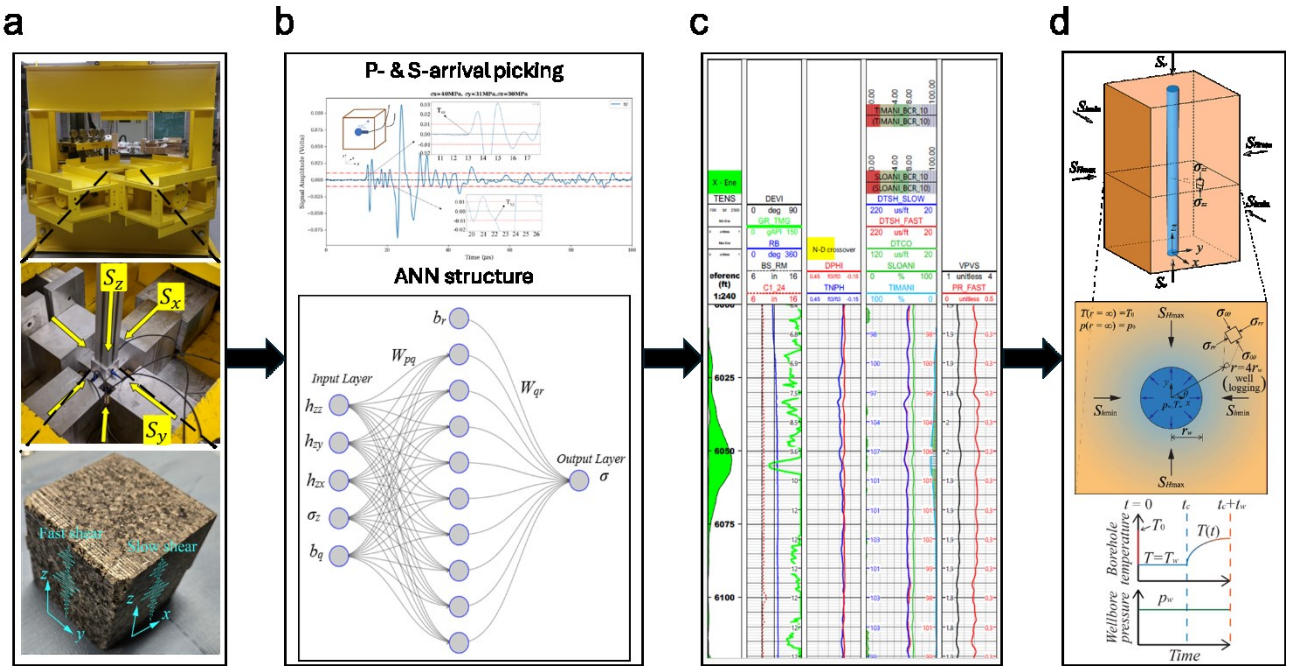

Figure 1: Workflow of the multi-component approach for characterizing in-situ stresses.

2.1 Core-based Laboratory TUV Experiment

Our approach begins with laboratory TUV experiments, which measured three acoustic velocities – P-wave, fast S-wave, and slow S-wave - under various true-triaxial stress conditions. Cubic rock samples (2.5 inches) from granitoid and gneiss formations of well 16A(78)-32 were precision-cut, ground, and saturated before applying confining stresses (Figure 1(a)). The experiments were performed using a hydraulic piston-actuated loading cell to apply true-triaxial confining stresses (with all three axes independently controlled). Initial hydrostatic loading up to 20 MPa was applied to prevent damage, followed by controlled deviatoric stress perturbations to obtain wave velocities under varying stress states.

Ultrasonic waves were generated and recorded by an active acoustic array consisting of three source-receiver sensor pairs (Olympus V153-RM ultrasonic transducers) in all tests, with each pair aligned with one of the three orthogonal directions (*x, y, z* in Figure 1(a)). To ensure proper contact and minimize damage, the transducers were coupled to the rock using glucose and rubber pads. Waveform data were recorded at a sampling rate of 10 MHz. These source-receiver pairs allowed us to measure the wave speed of the signals travelling between two facing source-receiver transducers. Specifically, the P-wave and both fast and slow S-wave velocities (presumably mutually orthogonal) were extracted from waveforms, with careful distinction between fast and slow S-wave polarities achieved by rotating the transducers by 90˚. This setup enabled the measurement of nine unique wave velocities for each stress condition, providing a robust dataset for subsequent analysis.

The premise of the TUV experiments is that stress anisotropy in subsurface rocks (i.e., difference in the three in-situ principal stresses) induces variations in wave velocities. Typically, wave velocities increase with rising stress levels. To distinguish between the two shear waves under a stress state of $S_x < S_y < S_z$, the fast and slow S-waves (propagating along *z*-axis) exhibit polarities aligned with the *y*- and *x*-axes, respectively (Figure 1(a)). By systematically measuring wave velocities under controlled stress states, the velocity-to-stress relationship of the tested rocks can be determined.

2.2 Predictive Velocity-to-Stress ML Model for Near-Field Stresses

Observations from core-based wave velocity measurements revealed close agreement with values obtained from sonic logs (Bunger et al., 2024). Taking advantage of these findings, we developed ML models using TUV test results and applied them to field logging data from Utah FORGE to estimate the near-field principal stresses (the minimum, intermediate, and maximum stresses) where sonic logging was conducted. Waveform data for all three wave types were analyzed, with first arrivals manually picked to ensure precision given the subtle velocity variations under stress. P-wave arrivals were identified at the initial upward inflection of the signal (T_{xx} in Figure 1(b)), while S-wave arrivals were determined using consistent crossings of a pre-set threshold (T_{xy} in Figure 1(b)). The slowness (the inverse of velocity, denoted by h_{ij}, in which i defines the wave propagation direction, and j indicates the signal polarity) for all three waves was calculated based on their travel times within the rock samples.

Supervised and unsupervised ML techniques were then applied to construct predictive models for assessing the in-situ stresses near a geothermal well. First, lab TUV data served as training inputs for the ML algorithms. Specifically, datasets comprising 41 TUV experiments on samples from well 16A(78)-32 were utilized to develop ML prediction models tailored to each well. Three input features, including h_{zz}, h_{zx}, and h_{zy}, were selected for training and testing/validating ML models for the vertical stress S_z. Then, the applied S_z was incorporated as an input feature, along with h_{zz}, h_{zx}, and h_{zy}, to train ML models for predicting the two orthogonal horizontal principal stresses corresponding to the fast and slow S-wave polarities, S_x and S_y.

This sequential workflow reflects the relevance of vertical stress (derived from gravitational and overburden forces) to the magnitude of horizontal stresses. Although slowness for all nine wave paths (one P- and two S-waves along each orthogonal direction) was measured, only the three slowness components (h_{zz}, h_{zx}, and h_{zy} in the case of a vertical well interval) corresponding to axial (z direction) wave propagation were used to develop the ML models. This approach aligns with the data available from sonic logging, which measures wave velocities in the axial direction of the wellbore.

An example of the Artificial Neural Network (ANN) architecture used in this study is shown in Figure 1(b). Key input features included ultrasonic wave slowness, while hyperparameters were optimized using grid search and k-fold cross-validation. The ANN model exhibited excellent predictive performance, achieving high accuracy and minimal error across all stress components. Additionally, unsupervised K-Means clustering was then employed to group subsurface rocks into distinct facies based on logging measurements such as gamma ray, porosity, and bulk density (Figure 1(c)). These clusters provided valuable insight into the geological structure/stratigraphic features of the vertical interval of the geothermal well. Finally, the trained ML models were applied to field logging data to predict local (near-field) principal stresses with high precision.

2.3 Physics-Based Model for Characterizing Far-Field Stresses Under Varying Thermo-Poro-Mechanical Conditions

It is worth noting that the ML model described earlier does not explicitly account for in-situ conditions, such as drilling and pre-cooling activities, as it assumes an intact rock formation without stress perturbations. However, sonic logging is conducted near the well, where strong poro-elastic stress alterations exist due to drilling. Furthermore, extensive circulation of cold fluid along the wellbore interval is often necessary for preventing downhole equipment used in well logging from overheating. These two major factors can interact (either amplifying or mitigating one another depending on the specific in-situ conditions) to significantly alter the near-wellbore stress field, potentially leading to misinterpretation of the in-situ stresses (Lu et al., 2024b). We will refer to these stress alterations as the induced thermo-poro-mechanical effect on the geothermal well. As a result, ML predictions may reflect the locally disturbed stresses caused by drilling and pre-cooling, rather than the true far-field confining stresses. Hence, it is necessary to model the thermo-poro-mechanical effects in the near-field and translate the stress field from the disturbed zone to the undisturbed far-field for accurate interpretation of logging data.

A schematic of a vertical wellbore drilled in a porous rock under stress and temperature boundary conditions (B.C.s) in 3D is shown in Figure 1(d). The problem is characterized by constant wellbore pressure and temperature along an interval of the well with radius, r_w. The wellbore is surrounded by a formation subjected to the minimum, intermediate, and maximum far-field principal compressive stresses ($S_{h\min} < S_{H\max} < S_v$). The constant temperature, T_w, is imposed at the borehole wall during pre-cooling, while the reservoir has a uniform initial temperature, T_0, and remains constant in far-field throughout the process. We denote the drop of temperature as $\Delta T = T_w - T_0$. Once pre-cooling stops (at $t = t_c$), the temperature boundary condition is removed, and the temperature field during both pre-cooling and the following warmup (at an arbitrary time $t = t_c + t_w$) stages can be solved by the finite element model (see an illustration of the temperature evolution on the borehole wall in Figure 1(d)). In addition, the reservoir is subjected to a uniform virgin pore pressure, p_0. Due to the excavation of the well, a constant mud pressure, p_w, is uniformly distributed along the borehole wall, resulting in a pressure difference, $\Delta p = p_w - p_0$. Consequently, the drilling/pre-cooling disturbed stress field is determined by (1) three far-field stresses, (2) mud pressure and pore pressure, and (3) thermal conditions during pre-cooling/warmup.

In the near-field, we adopted a cylindrical coordinate system (Figure 1(d)) defined by radius r, angle with respect to the minimum horizontal stress direction, θ, and axial depth z. Using this system, we calculated the three principal stress components predicted by the ML models: radial stress (σ_{rr}), tangential stress ($\sigma_{\theta\theta}$), and the axial stress (σ_{zz}). In this work, we imposed that the sonic logging measurements are taken at a location of $r = 4r_w$ (Figure 1(d)), a distance deemed appropriate based on the configuration of the ThruBit (through-the-bit) logging device utilized in well 16A(78)-32. Thanks to its linearity, the problem was decomposed into three distinct components for analysis:

I. **Near-wellbore stress concentration**: Resulting from excavation under mud pressure and far-field stresses.
II. **Poro-elastic stresses**: Induced by pore pressure diffusion near the well.
III. **Thermally induced stresses**: Generated by heat conduction during pre-cooling and warm-up.

We then used linear superposition to compute the total thermo-poro-elastic stresses (tension positive), written as

$$\sigma = \sigma^{\mathrm{I}} + \sigma^{\mathrm{II}} + \sigma^{\mathrm{III}} \tag{1}$$

Note that this linear superposition is valid under one important assumption: the thermally induced pore pressure in part III (not the pore pressure diffusion in part II) is negligible compared to all stress components in Equation 1, which has been verified by Lu et al. (2024b). Both drilling induced stress concentration (σ^{I}) under the mud pressure (p_w) and three far-field stresses ($S_{h\min}$, $S_{H\max}$, and S_v), and the poro-elastic stresses (σ^{II}) due to pressure diffusion can be solved using semi-analytical solutions (e.g., Cheng, 2016; Gao et al., 2016). For S^{I}, the three stress components can be computed by

$$\sigma_{\theta\theta}^{\mathrm{I}} = -\left(1+\frac{r_w^2}{r^2}\right)P_0 - \left(1+3\frac{r_w^4}{r^4}\right)S_0\cos 2\theta + \frac{r_w^2}{r^2}p_w \tag{2a}$$

$$\sigma_{rr}^{\mathrm{I}} = -\left(1-\frac{r_w^2}{r^2}\right)P_0 + \left(1-4\frac{r_w^2}{r^2}+3\frac{r_w^4}{r^4}\right)S_0\cos 2\theta - \frac{r_w^2}{r^2}p_w \tag{2b}$$

$$\sigma_{zz}^{\mathrm{I}} = -S_v - 4\nu\frac{r_w^2}{r^2}S_0\cos 2\theta \tag{2c}$$

in which $P_0 = \frac{S_{H\max}+S_{h\min}}{2}$, $S_0 = \frac{S_{H\max}-S_{h\min}}{2}$, and ν is the Poisson's ratio. Generally, ThruBit logging is conducted after the well has been drilled. The delay can be a few hours. Hence, we used the transient solutions for computing the poro-elastic stresses (part II). Given the constant pressure B.C.s ($p = p_w$ at borehole wall and $p = p_0$ in the far-field), the stresses and pore pressure were obtained in Laplace transform domain, denoted by $\tilde{S}^{\mathrm{II}}$ and $\tilde{p}^{\mathrm{II}}$. Their values are given by (Cheng, 2016)

$$\frac{s\tilde{\sigma}_{\theta\theta}}{p_w - p_0} = -2\eta\left[\frac{1}{r^*}\frac{\mathrm{K}_1\left(r^*\sqrt{s^*}\right)}{\sqrt{s^*}\mathrm{K}_0\left(\sqrt{s^*}\right)} - \frac{1}{r^{*2}}\frac{\mathrm{K}_1\left(\sqrt{s^*}\right)}{\sqrt{s^*}\mathrm{K}_0\left(\sqrt{s^*}\right)} + \frac{\mathrm{K}_0\left(r^*\sqrt{s^*}\right)}{\mathrm{K}_0\left(\sqrt{s^*}\right)}\right] \tag{3a}$$

$$\frac{s\tilde{\sigma}_{rr}}{p_w - p_0} = 2\eta\left[\frac{1}{r^*}\frac{\mathrm{K}_1\left(r^*\sqrt{s^*}\right)}{\sqrt{s^*}\mathrm{K}_0\left(\sqrt{s^*}\right)} - \frac{1}{r^{*2}}\frac{\mathrm{K}_1\left(\sqrt{s^*}\right)}{\sqrt{s^*}\mathrm{K}_0\left(\sqrt{s^*}\right)}\right] \tag{3b}$$

$$\frac{s\tilde{p}}{p_w - p_0} = \frac{\mathrm{K}_0\left(r^*\sqrt{s^*}\right)}{\mathrm{K}_0\left(\sqrt{s^*}\right)} \tag{3c}$$

where $r^* = \frac{r}{r_w}$, $s^* = \frac{r_w^2 s}{c}$ with s denoting the Laplace transform parameter, η and c are the poro-elastic stress coefficient and the consolidation coefficient, and K_0 and K_1 denote the modified Bessel function of the second kind of order 0 and 1, respectively. A numerical inversion method (Stehfest, 1970) was applied to evaluate the stress components in Equations 3(a,b,c). The overall pressure was then computed by $p^{\mathrm{II}} = p_\Delta^{\mathrm{II}} + p_0$. In addition, the axial stress under the plane-strain condition is expressed as

$$\sigma_{zz}^{\mathrm{II}} = \nu\left(\sigma_{\theta\theta}^{\mathrm{II}} + \sigma_{rr}^{\mathrm{II}}\right) - \alpha(1-2\nu)\left(p^{\mathrm{II}} - p_0\right) \tag{3d}$$

in which α is the Biot effective stress coefficient, computed by $\alpha = \frac{2\eta(1-\nu)}{1-2\nu}$. It is worthwhile to note that the ML stress predictions at well 16A(78)-32 are based on logging data collected along a vertical section of the well, including the compressional P-wave and fast and slow shear S-wave velocities under stress induced anisotropy in the surrounding rock. In this case, all waves propagate along the axial direction of the well, and the two shear waves polarize orthogonally to the well axis. Thus, ML predicted near-field principal stresses (S_1, S_2 and S_3) correspond to the vertical and two mutually orthogonal horizontal stresses (σ_{zz}, σ_{rr} and $\sigma_{\theta\theta}$), and Equations 1-3 are valid for our thermo-poro-elastic stress analysis of 16A(78)-32. For an inclined well, stress transformation is needed.

Next, the finite element model was developed in Abaqus to compute the radial heat conduction and its induced thermal stresses, σ^{III}. Two subproblems were solved sequentially:

Subproblem 1: Pre-cooling and warmup lead to temperature change near the borehole. To model the heat transfer from the borehole to the reservoir, the cold fluid circulation, characterized by constant temperatures at borehole wall ($T = T_w$ at $r = r_w$) and far-field ($T = T_0$

at r =2.5 m), begins at $t = 0$ and ends at t_c. The warmup duration with fixed far-field temperature (T_0) is characterized by t_w (Figure 1(d)).

Subproblem 2: After obtaining the temperature field associated with pre-cooling/warmup, we then imposed this temperature distribution as a pre-defined field variable in a thermo-mechanical problem setup. The resulting thermo-elastic stress fields caused by heat transfer in reservoir was then computed.

The problem of pre-cooling/warmup induced stresses surrounding a circular wellbore was solved using a one-way coupled setup (heat transfer causes mechanical deformation but the deformation in rocks does not affect the temperature distribution). The entire problem was modeled in a 2.5-m radius circular domain (Figure 2). Mesh in areas near the borehole was refined to capture the expected sharp stress/strain gradient. A total of 19,521 nodes and 6,400 elements were generated. For the heat transfer subproblem 1, the heat transfer was modeled with DC2D8 elements (8-node quadratic heat transfer quadrilateral element). For the thermo-mechanical subproblem 2, we used CPE8 (8-node biquadratic plane strain quadrilateral element).

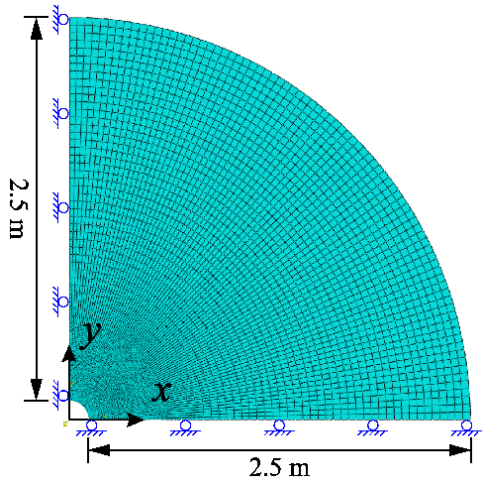

Figure 2: Mesh and B.C.s of both subproblems generated in Abaqus.

3. RESULTS

3.1 ML Predictions for Near-Field Principal Stresses

TUV data from core samples were used to train and test the ML models. Rock facies were determined using the rock properties obtained from well logging, including neutron porosity (NPHI), gamma ray (GR), and bulk density (ρ). An example of these measurements, along with wave slownesses, within the depth interval of 5,000-6,000 ft at well 16A(78)-32 is displayed in Figure 3(a). A total of five rock facies were found within this interval, indicating the heterogeneous nature of subsurface rock formations (more details are provided in Mustafa et al., 2024). The near-wellbore principal stresses were predicted by the ANN models using same logging data from the vertical section (Figure 3(b)). The predicted stresses were compared with field estimation of the in-situ stresses. The ML predicted maximum compressive stress S_1 was compared with bulk density gradient - based vertical stress, whereas the intermediate and minimum compressive stresses (S_2 and S_3) were compared with field estimation of the maximum and minimum horizontal stresses based on elastic geomechanical model, respectively.

As discussed in Section 2, strong near-wellbore stress concentration and thermo-poro-elastic stress disturbance are likely present at the time and location of logging data collection. Consequently, the three principal stresses predicted by the ML model using the log data in near-field need to be translated to the far-field stresses ($S_{h\min}$, $S_{H\max}$, and S_v) using physics-based modeling through thermo-poro-mechanical coupling under the relevant in-situ conditions. Despite these complexities, comparisons show that the ML predicted stresses align closely with the vertical stress inferred from the bulk density gradient and the horizontal stresses derived from elastic geomechanical models, particularly at depths where core samples were extracted and tested in TUV experiments (indicated by green circles in Figure 3(b)). The ML predicted stresses at two locations of extracted core samples (depths 5,474 and 5,850 ft) are summarized in Table 1.

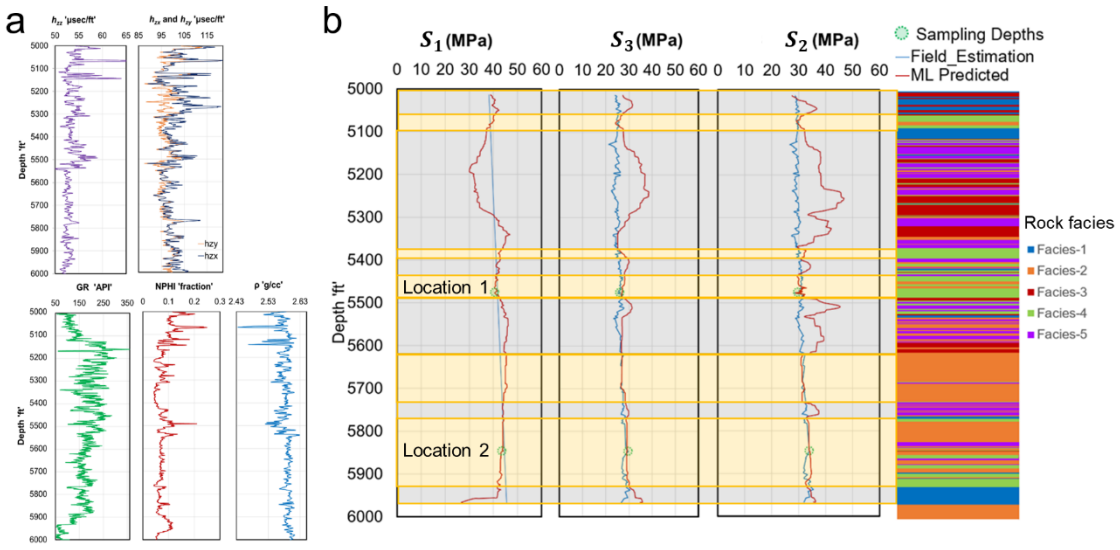

Figure 3: Measurements from well logging at 16A(78)-32 (a) and ML predicted near-field principal stresses (b), noting that prediction in the grey shaded zones are not valid because the model was not trained on rock type from that zone.

Table 1: Principal stresses by ML models for well 16A(78)-32 and wellbore and virgin pore pressure used in the numerical model. The location with superscript (*) was investigated in the thermo-poro-elastic stress analysis.

Ture vertical depth	5,474 ft (#1)	5,850 ft* (#2)
ML predicted maximum stress (S_1)	41 MPa	43.1 MPa
ML predicted intermediate stress (S_2)	31 MPa	34.2 MPa
ML predicted minimum stress (S_3)	27.1 MPa	29 MPa
Wellbore pressure (p_w) (mud weight 9.5 ppg)	18.7 MPa	19.9 MPa
Virgin pore pressure (p_0)	16.4 MPa	17.5 MPa

3.2 Characterizing Far-Field Stress Fields by Physics-Based Modeling

To account for the impact of near-wellbore thermo-poro-elastic stress alterations, we then imposed the ML predictions as the near-field stresses (at $r = 4r_w$) and solved for the far-field stresses under varying drilling/pre-cooling conditions. To demonstrate the induced thermo-poro-mechanical effects, we studied the stresses at one location (#2) with the depth of 5,850 ft (Table 1). The stress analysis incorporated realistic material properties of granitic rocks and considered both pre-cooling and warmup scenarios, as outlined in Table 2. Specifically, we investigated a scenario involving a 10-hour pre-cooling circulation conducted after the borehole was drilled with a temperature drop of 40 ˚C ($T_0 - T_w$), followed by a waiting (warmup) period lasting up to 4 hours. Logging activities were assumed to take place either immediately following the pre-cooling stage or at the end of the 4-hour warmup phase (corresponding to a total elapsed time of 14 hours after drilling).

Table 2: Input parameters.

Young's modulus (E)	37.5 GPa
Poisson's ratio (ν)	0.25
Density (ρ)	2710 kg/m^3
Thermal conductivity (k_T)	2.5 W/(m·K)
Volumetric thermal expansion coefficient (β_d)	8×10^{-6} K^{-1}
Consolidation coefficient (c)	2.15×10^{-5} m^2/s
Poro-elastic stress coefficient (η)	0.08

Biot effective stress coefficient (α)	0.24
Reservoir temperature (T_0)	150 ˚C
Pre-cooling temperature (T_w)	110 ˚C
Pre-cooling duration (t_c)	10 hours
Warmup duration (t_w)	4 hours
Wellbore radius (r_w)	0.12 m

3.2.1 Determining the location with largest stress-induced wave speed anisotropy

All three components of the thermo-elastic stresses ($\sigma_{\theta\theta}^{\mathrm{III}}$, $\sigma_{rr}^{\mathrm{III}}$, and $\sigma_{zz}^{\mathrm{III}}$ obtained in Abaqus simulations) exhibit axisymmetry due to the radial nature of heat conduction, resulting in their independence from the angular coordinate, θ. Making use of this symmetry, we modeled a quarter of the circular domain. Two drilling/pre-cooling scenarios were explored - 10-hour pre-cooling followed by 4-hour warmup. Figure 4 displays the distributions of the temperature and $\sigma_{xx}^{\mathrm{III}}$ at the end of both stages. While $\sigma_{zz}^{\mathrm{III}}$ was obtained directly from Abaqus simulations, $\sigma_{\theta\theta}^{\mathrm{III}}$ and $\sigma_{rr}^{\mathrm{III}}$ were determined using the relationships: $\sigma_{\theta\theta}^{\mathrm{III}} = \sigma_{xx}^{\mathrm{III}}\left(\theta = \frac{\pi}{2}\right)$ and $\sigma_{rr}^{\mathrm{III}} = \sigma_{xx}^{\mathrm{III}}(\theta = 0)$.

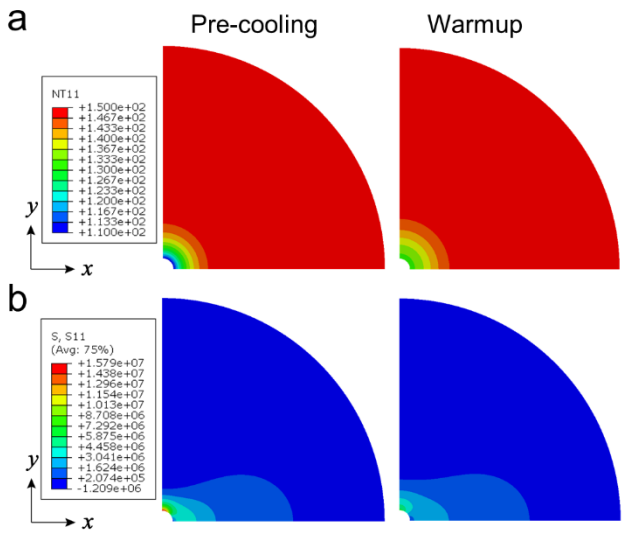

Figure 4: Distribution of temperature (a) and $\sigma_{xx}^{\mathrm{III}}$ (b) at the end of pre-cooling and warmup periods.

Additionally, poro-elastic stresses (σ^{II}) induced by radial pore pressure diffusion are also axisymmetric. Only σ^{I} (drilling induced stress concentration) varies with $\theta \in \left[0, \frac{\pi}{2}\right]$. The key question then became identifying the specific value of θ at a fixed distance to well ($r = 4r_w$) where P- and fast and slow S-waves correspond (i.e., the location that exhibits the greatest stress-induced wave speed anisotropy). According to Equation 2, all three stresses, $\sigma_{\theta\theta}^{\mathrm{I}}$, σ_{rr}^{I}, and σ_{zz}^{I}, exhibit monotonic trends, either increasing or decreasing with θ. Thus, the most pronounced stress-induced wave speed anisotropy occurs at the extreme stress values, which are recovered at either $\theta = 0$ or $\theta = \frac{\pi}{2}$. Further investigation into the stress magnitudes using realistic far-field stress values revealed that both the least and greatest compressive stresses occur at $\theta = 0$ - $\sigma_{\theta\theta}^{\mathrm{I}}(\theta = 0) < \sigma_{rr}^{\mathrm{I}}\left(\theta = \frac{\pi}{2}\right) < \sigma_{\theta\theta}^{\mathrm{I}}\left(\theta = \frac{\pi}{2}\right) < \sigma_{rr}^{\mathrm{I}}(\theta = 0)$ for $r = 4r_w$ (tension positive). To summarize, values of the near-field stresses ($\sigma_{\theta\theta}$, σ_{rr}, and σ_{zz}) at $r = 4r_w$, $\theta = 0$ align with the ML predictions for the three principal compressive stresses:

$$S_3 = -\sigma_{rr}\left(r = 4r_w, \theta = 0\right),\ S_2 = -\sigma_{\theta\theta}\left(r = 4r_w, \theta = 0\right),\ S_1 = -\sigma_{zz}\left(r = 4r_w, \theta = 0\right).$$

Therefore, ML predicted near-field stresses under the influences of stress concentration and axi-symmetric pore pressure diffusion and heat transfer were imposed at this location to solve for the entire stress field.

3.2.2 Translating near-field ML predictions to far-field stresses under various thermal conditions

By imposing these ML predictions as the pre-determined near-field stresses, we solved the inverse problem to find the corresponding far-field stresses under two scenarios: (1) logging (and its associated ML predictions) conducted immediately after a 10-hour pre-cooling circulation, and (2) logging performed following an additional 4-hour warmup period after the 10-hour pre-cooling (a total of 14 hours). The far-field principal stresses were determined by iteratively adjusting all three far-field stresses to achieve agreement with the ML predicted stresses in near-field for each scenario. At the depth of 5,850 ft, the near-field stresses were S_3=27 MPa, S_2=30.2 MPa, S_1=41.1 MPa (Table 1). The translated far-field stress values are presented in Figure 5, which compares the ML-predicted near-field stresses with the estimated far-field stresses. In both scenarios, the vertical stress (S_v) in far-field is notably higher than the ML prediction (S_1), reflecting the impact of the near-field stress concentration. Additionally, both pre-cooling and warmup scenarios indicate more isotropic horizontal stress states compared to the ML-predicted near-field stresses. This shift toward isotropic stress states is attributed to thermally induced tensile stresses, which are most pronounced immediately after pre-cooling. These tensile stresses gradually dissipate during the warmup period.

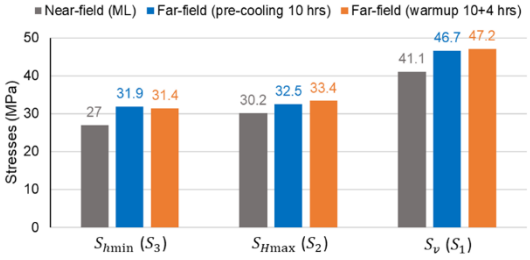

Figure 5: Comparison of ML predicted near-field stresses and translated far-field stresses in two pre-cooling scenarios.

Figure 6 further illustrates the distribution of all three stresses along the radial trajectory of $\theta = 0$ emanating from the borehole. Significant thermal effect is observed at the borehole wall, particularly in the tangential stress, $\sigma_{\theta\theta}$, which exhibits a variation exceeding 12 MPa between the pre-cooling and warmup scenarios. The impact of thermo-poro-elastic stress alterations diminishes with increasing distance from the borehole and becomes negligible at a radius of approximately 1 m.

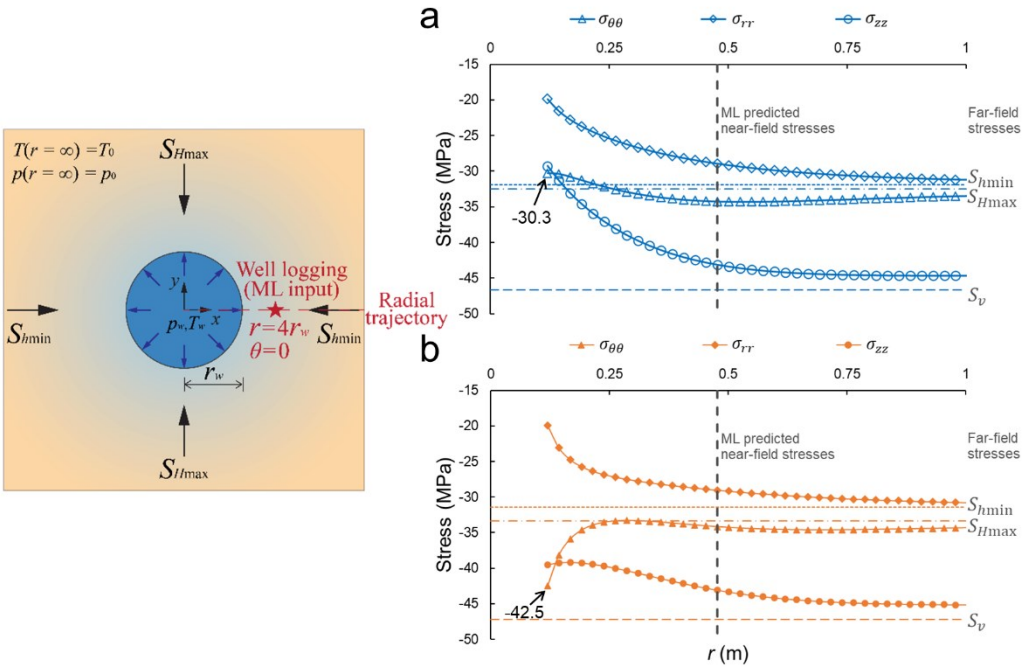

Figure 6: Distribution of stresses along the radial trajectory of $\theta = 0$ in two scenarios: (a) immediately after 10-hour borehole pre-cooling circulation, and (b) another 4-hour waiting period. ML predicted stresses in near-field ($r = 4r_w$) were imposed to solve for the three far-field stresses ($S_{h\min}$, $S_{H\max}$, S_v) in both scenarios.

4. CONCLUSION

This study presents a multi-component approach for in-situ stress characterization near geothermal wells by combining lab and field data, ML and physics-based modeling. Lab TUV experiments establish the velocity-to-stress relationships in subsurface rocks exhibiting

substantial stress induced wave speed anisotropy, which enables ML models to predict near-field stresses from sonic logging data. Then, thermo-poro-mechanical effect, induced by near-wellbore stress concentrations and drilling/pre-cooling induced thermal stresses, is taken into consideration using finite element simulations to translate the ML-derived near-field principal stresses into far-field stresses.

Our results indicate that thermal effects play a critical role in stress distribution, with significant variations in tangential stress near the borehole in varying drilling/pre-cooling scenarios. The thermo-poro-elastic stress alterations diminish with increasing radial distance and time. Additionally, thermo-poro-mechanical coupling amplifies differences between horizontal principal stresses in the near-field, while far-field stresses are generally more isotropic.

This integrated framework demonstrates a robust methodology for accurate far-field stress characterization around vertically drilled geothermal wells and can be extended to inclined wells by appropriately transforming stress components across different orientations. Our findings provide critical insights for optimizing the design and development of enhanced geothermal systems and other geo-energy applications.

ACKNOWLEDGEMENTS

This work was performed at the University of Pittsburgh with funding provided by DOE EERE Geothermal Technologies Office to Utah FORGE and the University of Utah under Project DE-EE0007080 Enhanced Geothermal System Concept Testing and Development at the Milford City, Utah Frontier Observatory for Research in Geothermal Energy (Utah FORGE) site.

REFERENCES

Bunger, A., Higgins, J., Huang, Y., Hartz, O., and Kelley, M. (2024). Integration of triaxial ultrasonic velocity and deformation rate analysis for core-based estimation of stresses at the Utah FORGE geothermal site. Geothermics, 120, 103008.

Cheng, A. H. D. (2016). Poroelasticity. Springer.

Gao, Y., Liu, Z., Zhuang, Z., Hwang, K. C., Wang, Y., Yang, L., and Yang, H. (2016). Cylindrical borehole failure in a poroelastic medium. Journal of Applied Mechanics, 83(6), 061005.

Lu, G., Kelley, M., Raziperchikolaee, S., and Bunger, A. (2024a). Modeling the impact of thermal stresses induced by wellbore cooldown on the breakdown pressure and geometry of a hydraulic fracture. Rock Mechanics and Rock Engineering, 57 (2024): 5935–5952.

Lu, G., Lu, Y., Kelley, M., Raziperchikolaee, S., and Bunger, A. P. (2024b). Thermo-poro-elastic stress alteration around an EGS well due to cold fluid circulation. In 58th US Rock Mechanics/Geomechanics Symposium, Golden, Colorado, 23–26 June 2024. ARMA-24-689.

Mustafa, A., Kelley, M., Lu, G., and Bunger, A. P. (2024). An integrated machine learning workflow to estimate in situ stresses based on downhole sonic logs and laboratory triaxial ultrasonic velocity data. Journal of Geophysical Research: Machine Learning and Computation, 1(4), e2024JH000318.

Prioul, R., Bakulin, A., and Bakulin, V. (2004). Nonlinear rock physics model for estimation of 3D subsurface stress in anisotropic formations: theory and laboratory verification. Geophysics, 69(2), 415–425.

Sinha, B. K., and Kostek, S. (1996). Stress-induced azimuthal anisotropy in borehole flexural waves. Geophysics, 61(6), 1899-1907.

Stehfest, H. (1970). Numerical inversion of Laplace transforms. Communications of the ACM, 13:47–49.

Zang, A., and Stephansson, O. (2009). Stress field of the earth's crust. Springer.